

MULTIVARIATE CLUSTER POINT PROCESS MODEL: PARENT LOCATION IMPROVES INFERENCE FOR COMPLEX BIOFILM IMAGE DATA

BY SUMAN MAJUMDER^{1,a}, BRENT A. COULL^{1,b} JESSICA L. MARK WELCH^{2,d}
PATRICK J. LA RIVIERE^{3,c} FLOYD E. DEWHIRST^{4,f}
JACQUELINE R. STARR^{5,*g} AND KYU HA LEE^{1,*c}

¹Harvard T. H. Chan School of Public Health, Boston, Massachusetts, U.S.A., ^asmajumder@hsph.harvard.edu;
^bbcoull@hsph.harvard.edu; ^cklee@hsph.harvard.edu

²Marine Biological Laboratory, Woods Hole, Massachusetts, U.S.A., ^djmarkwelch@mbl.edu

³University of Chicago, Chicago, Illinois, U.S.A., ^epjlarivi@uchicago.edu

⁴The Forsyth Institute, Cambridge, Massachusetts, U.S.A., ^ffdewhirst@forsyth.org

⁵Brigham and Women's Hospital, Boston, Massachusetts, U.S.A., ^gspjst@channing.harvard.edu

A common challenge in spatial statistics is to quantify the spatial distributions of clusters of objects. Clusters of similar or dissimilar objects are encountered in many fields, including field ecology, astronomy, and biomedical imaging. Frequently used approaches treat each cluster's central object as latent, but it is often the case that cells of one or more types cluster around cells of another type. Such arrangements are common, for example, in microbial biofilm, in which close interspecies spatial clustering is thought to reflect physical interactions among species. Because these interactions arise from or drive biofilm community structure, quantifying these spatial relationships may provide clues to disease pathogenesis or treatment effects. Even when clustering arrangements are not strictly parent-offspring relationships, treating the central object as a parent can enable use of parent-offspring clustering frameworks. We proposed a novel, fully Bayesian, multivariate spatial point process model to quantify multi-cellular arrangements with parent-offspring statistical approaches. We used the proposed model to analyze data from a human dental plaque biofilm image containing spatial locations of *Streptococcus*, *Porphyromonas*, *Corynebacterium*, and *Pasteurellaceae*, among other species. The proposed multivariate cluster point process (MCP) model departs from commonly used approaches in that it exploits the locations of the central parent object in clusters. It also accounts for possibly multilayered, multivariate parent-offspring clustering. In simulated datasets, the MCP outperforms the classical Neyman-Scott process model, a univariate model for modeling spatially clustered processes, by producing decisively more accurate and precise parameter estimates. Applied to the motivating biofilm data, we quantified the simultaneous clustering of *Streptococcus* and *Porphyromonas* around *Corynebacterium* and of *Pasteurellaceae* around *Streptococcus*. The proposed MCP model successfully captured the parent-offspring structure for all the taxa involved.

1. Introduction. Instances abound in nature where one type of object is dispersed around another type of object. At interplanetary and field ecologic scales, respectively, radio galaxies

*Co-senior authors

Keywords and phrases: dental plaque sample, imaging, microbiome, parent-offspring models, point processes, spatial statistics, Thomas process.

(Yates, Miller and Peacock, 1989; Hill and Lilly, 1991) (Bornancini et al., 2004, 2006) and forest songbirds (Tarof and Ratcliffe, 2004; Bourque and Desrochers, 2006; Melles et al., 2009) exemplify this type of spatial clustering. At microscopic scales, among single-celled organisms and human cells, such arrangements are common. For example, in human dental plaque biofilm, spherical *Streptococcus* cells often cluster around the ends of filamentous *Corynebacterium* cells (Jones, 1972; Mark Welch et al., 2016). These corn-cob-like arrangements have been observed in dental plaque for decades and are likely to hold clues about interspecies microbial interactions. To describe and quantify such arrangements, we have developed a new multivariate cluster point process model (MCP).

Most biofilm image analysis approaches have focused on macro-level structural characteristics or derived features, such as biofilm volume, thickness, or surface roughness (Daims, Lückner and Wagner, 2006; Vorregaard, 2008; Hartmann et al., 2021). Less commonly, spatial point process models have been used to analyze the spatial patterning of microbial cells: how cells of one taxonomic class (or taxon) are distributed in relation to other cells of the same or different taxa. However, standard point process models, such as the log-Gaussian Cox process model (Møller, Syversveen and Waagepetersen, 1998), do not account for the complex spatial clustering arrangements often present in biofilm images. Methods that can account for such complexity are needed not only to quantify the visible arrangements but also because there may be other spatially dependent arrangements that, unlike the “corn-cobs,” are not visually discernable. Quantification, in turn, would allow benchmarking and hypothesis testing, such as for comparing effects of an antibacterial treatment on biofilm architecture.

The Neyman-Scott process model (NSP) (Neyman and Scott, 1958) is a classic statistical model used to quantify spatially dependent clustering relationships, most often applied to actual parents and offspring (such as trees in a forest). In this approach, locations of the central object in each cluster are treated as latent, in part because in a cluster comprising similar objects (such as a grove of trees or a school of fish), it may be impossible to identify any true parent individuals. In contrast, in corn-cob arrangements in dental plaque biofilm, the locations of the central “parent” *Corynebacterium* cells are often known. Though reasonable for within-taxon clustering, naïve application of the NSP model to investigate between-taxon relationships (i.e. one taxon clustering around the other) is inappropriate because it ignores the taxon in the center of the clusters.

Corn-cob arrangements in dental plaque biofilm have other characteristics that preclude direct application of the NSP model or the related shot noise Cox process model (Møller, 2003). First, the “parent” and “offspring” cells are of different bacterial taxa, thus requiring a multivariate extension of univariate approaches. Second, the corn-cob arrangements sometimes include multiple “offspring” taxa in that both *Streptococcus* and *Porphyromonas* are observed around *Corynebacterium* “parents.” In this regard, existing multivariate cluster point process models (Tanaka and Ogata, 2014; Jalilian et al., 2015) are not applicable to microbial corn-cob-like arrangements because they do not model the taxa in the cluster center and have no scope to enforce multiple offspring taxa’s having the same parent taxon. To our knowledge, existing approaches fail to address a third challenge, that the corn-cobs can be multilayered in nature (e.g., Figure 1). And, fourth, the corn-cob arrangements themselves are part of a more complexly organized microbial community that includes other taxa unrelated to the arrangements.

The primary innovation of the proposed MCP model is that it exploits the known locations of central objects in clusters. It also addresses the above-described challenges. Specifically, it can quantify multivariate and multilayered clustering and inter-process relationships. The MCP is flexible in that it can simultaneously model clustered and non-clustered processes

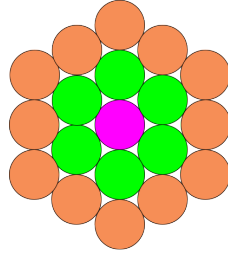


Fig 1: A multi-layered parent-offspring structure. The green dots behave as offspring to the pink dot while the orange dots behave as offspring to the green dots

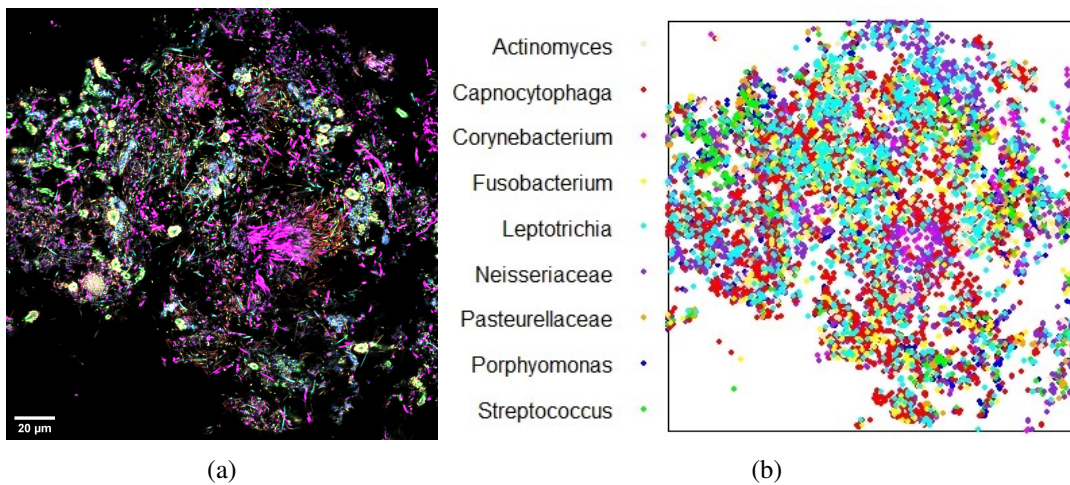


Fig 2: (a) A biofilm image of a dental plaque sample from from a human donor: RGB image - taxa relevant to the multilayered concob arrangements are *Corynebacterium* (Pink), *Streptococcus* (Green), *Porphyromonas* (Blue) and *Pasteurellaceae* (Orange); (b) post-segmentation spatial locations of the centroids of cells identified via genus-specific probes, as indicated

and can be applied in multivariate (multi-taxon) or univariate (individual taxon) contexts. In this paper, we describe the model in detail, evaluate its performance through simulation studies, and demonstrate the feasibility of applying the model to both real and synthetic datasets.

2. Microbiome Biofilm Image Data from Dental Plaque Samples. We carried out a re-analysis of existing image data from [Mark Welch et al. \(2016\)](#) in which dental plaque samples were collected, embedded in methacrylate, sectioned, and subjected to multi-spectral fluorescence *in situ* hybridization (FISH) and imaging. Multiple genus- and family-level probes were applied simultaneously to identify *Actinomyces*, *Capnocytophaga*, *Corynebacterium*, *Fusobacterium*, *Leptotrichia*, *Neisseriaceae*, *Pasteurellaceae*, *Porphyromonas*, and *Streptococcus*. The near-universal probe Eub338 targeting most bacteria was also included (Figure 2(a)). We performed segmentation of the biofilm image in FIJI ([Schindelin et al., 2012](#)) by applying a 3×3 median filter and “Auto Local” thresholding function with the Bersen method. Spatial coordinate information for centroids of the taxa was identified by applying the “An-

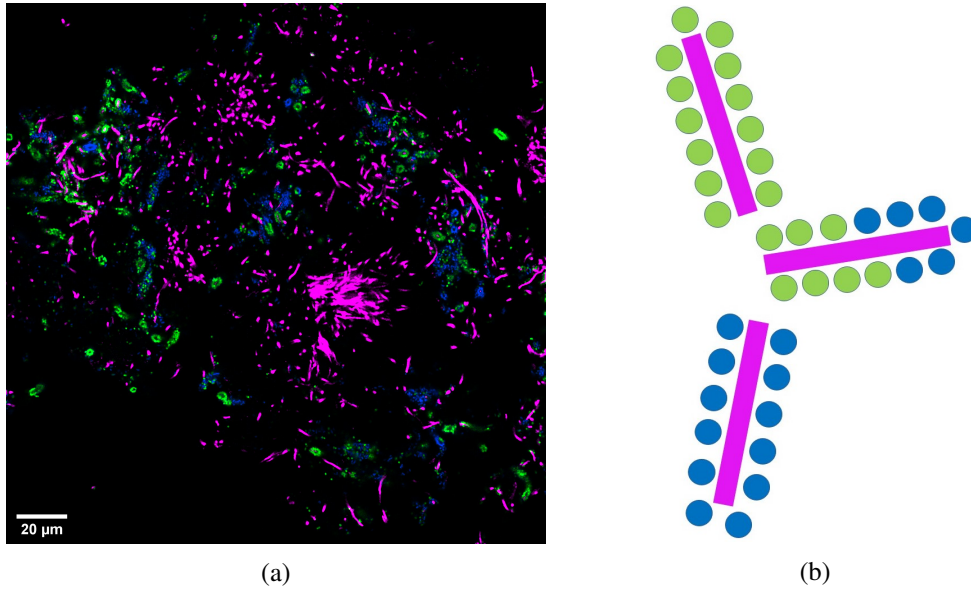


Fig 3: (a) The same image as in Figure 2, displaying channels corresponding to *Corynebacterium* (Pink), *Streptococcus* (green) and *Porphyromonas* (Blue); and (b) cartoon depicting various corncob structures visible in the image. The corncob structures are present in areas of the image corresponding to the tip of the *Corynebacterium*. At the center of the dense clump of *Corynebacterium* in (a), no corncobs are observed. For other examples of biofilm images with corncob structures in which both *Streptococcus* and *Porphyromonas* cells cluster around the same *Corynebacterium* cell, see Supplemental Figure S2, panel C, in [Mark Welch et al. \(2016\)](#).

alyze Particles” function using a size filter with a $0.5 \mu\text{m}$ diameter threshold in FIJI (Figure 2(b)).

The sampled image is representative of similar samples from the same and other donors without active tooth decay (not shown). Filamentous *Corynebacterium* cells (Figure 3, pink) are common. Members of this genus are now believed to help establish the “healthy” dental microbiota, providing a scaffold around which other community members assemble. In some parts of the image, cells of *Streptococcus* (Figure 3, green) and *Porphyromonas* (Figure 3, blue) seem to surround the tips of *Corynebacterium* filaments ([Mark Welch et al., 2016](#)), sometimes with both *Streptococcus* and *Porphyromonas* in the same clusters. Adding another layer and further complexity, *Pasteurellaceae* cells (Figure 4, orange) sometimes surround *Streptococcus* cells ([Mark Welch et al., 2016](#); [Morillo-Lopez et al., 2021](#)). As outlined in Section 1, these arrangements give *Streptococcus* the potential to be either parent, offspring, or both in the same cluster. Other taxa are scattered around seemingly homogeneously and may or may not have additional spatial relationships with *Corynebacterium*, *Streptococcus*, *Porphyromonas*, or *Pasteurellaceae* (individual images in Section B of the Supplementary Materials).

3. Multivariate Cluster Point Process Model. We consider a multivariate process Y to be a collection of processes Y_i , $i = 1, \dots, m$, at location $\mathbf{s} \in \mathcal{W} \subset \mathbb{R}^2$, where each component Y_i is a Poisson process characterized by an intensity function $\lambda_i(\mathbf{s})$ and \mathcal{W} , the observation window. In application to the biofilm sample, each Y_i will capture the spatial distribution of

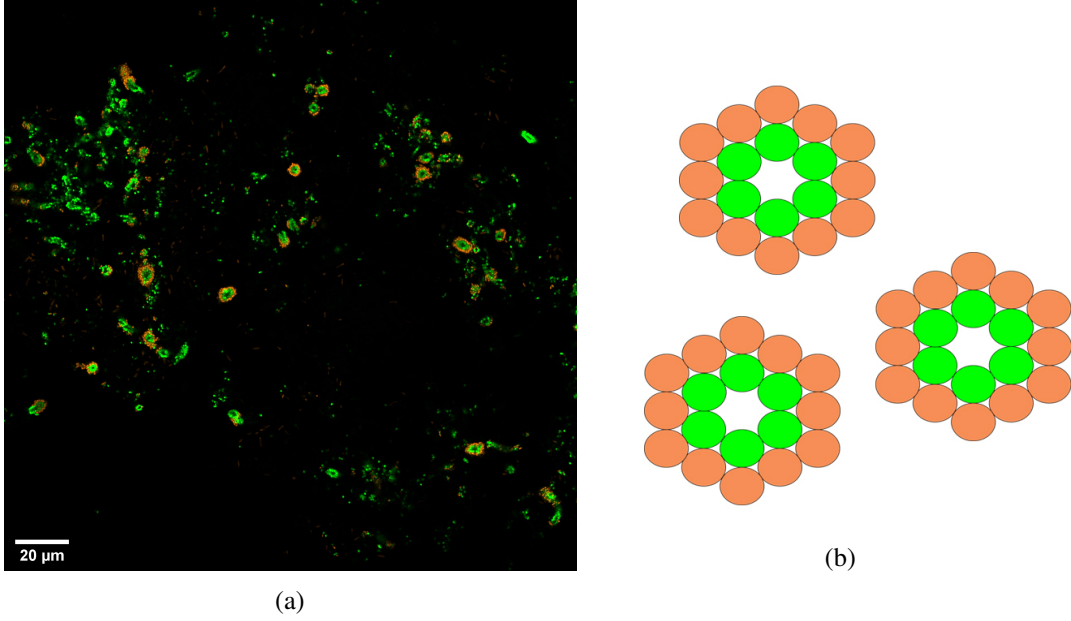


Fig 4: (a) The same image as in Figure 2, displaying channels corresponding to *Pasteurellaceae* (Orange) and *Streptococcus* (Green); and (b) a cartoon image illustrating the clustering of *Pasteurellaceae* around *Streptococcus*. Hiding the pink *Corynebacterium* channels highlights the outer layer in the multilayer arrangements.

a taxon, i . The intensity function $\rho(\mathbf{s})$ of the superimposed process is defined as

$$(1) \quad \rho(\mathbf{s}) = \sum_{i=1}^m \lambda_i(\mathbf{s}) \mathbb{I}(\mathbf{s} \in Y_i),$$

where $\mathbb{I}(\mathbf{s} \in Y_i)$ is the indicator function of the i -th process being observed at location $\mathbf{s} \in \mathcal{W}$. The indicator terms ensure that only one process can be observed at each location.

3.1. Model Formulations. Suppose that Y_1, \dots, Y_p , are homogeneous Poisson processes with intensities λ_v^C for $v = 1, \dots, p$ ($< m$) and serve only as parent processes (“C” signifies central objects, or parents). Then we consider the q ($\leq m - p$) processes, Y_{p+1}, \dots, Y_{p+q} , that behave as offspring processes. Each offspring process is assumed to have one parent process. Let C_l for $l = p + 1, \dots, p + q$ denote the corresponding parent processes for offspring process Y_l with the following properties:

- i) If offspring processes Y_l and $Y_{l'}$, $l \neq l'$ share a parent process, then $C_l = C_{l'}$;
- ii) If an offspring process Y_j serves as a parent process for another offspring process Y_l for some l and $j = p + 1, \dots, p + q$, then $C_l = Y_j$.

We assume that the offspring points are distributed around parent point $\mathbf{c} \in C_l$, $l \in \{p + 1, \dots, p + q\}$ according to the rule $\alpha_l k_l(\cdot - \mathbf{c}, h_l)$, where α_l is the average number of offspring per parent, $k_l(\cdot, \cdot)$ is a kernel (e.g. Gaussian), and h_l is a bandwidth parameter that controls the distance between the parent and its offspring locations for the l -th offspring process (Chiu et al., 2013; Illian et al., 2008). The parameter h_l should be interpreted as the distance at which offspring are most likely to be situated relative to their corresponding parents. The remaining $m - p - q$ types (e.g. taxa) that are unrelated to multilayered arrangements are

modeled as homogeneous Poisson processes with intensities λ_j for $j = p + q + 1, \dots, m$. Therefore, under the proposed specification, the intensity function in (1) can be written as

$$(2) \quad \rho(\mathbf{s}) = \sum_{v=1}^p \lambda_v^C \mathbb{I}(\mathbf{s} \in Y_v) + \sum_{l=p+1}^{p+q} \alpha_l \sum_{\mathbf{c}_l \in C_l} k_l(\mathbf{s} - \mathbf{c}_l, h_l) \mathbb{I}(\mathbf{s} \in Y_l) + \sum_{j=p+q+1}^m \lambda_j \mathbb{I}(\mathbf{s} \in Y_j).$$

Since the superimposed process Y is modeled as a Poisson process with intensity function $\rho(\mathbf{s})$ in (2), the likelihood as a function of the unknown parameters $\boldsymbol{\theta} = \{\alpha_{p+1}, \dots, \alpha_{p+q}, h_{p+1}, \dots, h_{p+q}, \lambda_1^C, \dots, \lambda_p^C, \lambda_{p+q+1}, \dots, \lambda_m\}$, is given by

$$(3) \quad L(Y|\boldsymbol{\theta}) = \exp \left\{ \int_{\mathcal{W}} 1 - \rho(\mathbf{u}) \mathbf{d}\mathbf{u} \right\} \prod_{\mathbf{y} \in Y} \rho(\mathbf{y}) \\ \propto \exp \left\{ |\mathcal{W}| - \sum_{v=1}^p |\mathcal{W}| \lambda_v^C - \sum_{l=p+1}^{p+q} \alpha_l \sum_{\mathbf{c}_l \in C_l} \int_{\mathcal{W}} k_l(\mathbf{u} - \mathbf{c}_l, h_l) \mathbf{d}\mathbf{u} - \sum_{j=p+q+1}^m |\mathcal{W}| \lambda_j \right\} \\ \times \exp \left\{ \sum_{v=1}^p n_v \log \lambda_v^C + \sum_{l=p+1}^{p+q} \sum_{\mathbf{y} \in Y_l} \log \left(\alpha_l \sum_{\mathbf{c}_l \in C_l} k_l(\mathbf{y} - \mathbf{c}_l, h_l) \right) + \sum_{j=p+q+1}^m n_j \log \lambda_j \right\},$$

where $|\mathcal{W}|$ is the area of \mathcal{W} , and n_i denotes the number of observations from the i -th process in \mathcal{W} .

3.2. Quantities of Interest. Ripley's $K(r)$ function (Ripley, 2005; Diggle et al., 2013; Cressie, 2015) for a stationary point process is defined as the expected number of neighbors of a typical point from the process that lies within distance r from the said point, divided by the intensity of the process. In practice, we compute the empirical $K(r)$ function as

$$(4) \quad \hat{K}(r) = \frac{|\mathcal{W}|}{n(n-1)} \sum_{i=1}^n \sum_{j=1, j \neq i}^n \mathbb{I}(d_{ij} \leq r),$$

or its edge-corrected version, where d_{ij} is the distance between points i and j in the process realization with n points. This standardized tool allows point patterns to be compared and their spatial correlations to be quantified. For clustered processes, the $K(r)$ is expected to be higher than πr^2 , at least for smaller values of r . The $K(r)$ therefore provides an indication spatial clustering. Some drawbacks include the assumption of the process's homogeneity and the fact that lack of correlation does not imply that the process is not clustered.

In typical Neyman-Scott processes, when the parent processes are unobserved, the $K(r)$ provides a useful way to quantify clustering of the offspring process. In contrast, in multi-process contexts, the $K(r)$ is less useful: the homogeneity assumption is violated, and the $K(r)$ fails to provide any measure of inter-process relationship. Computing the $K(r)$ for the superimposed process Y , as in Section 3.1, would require the computation of the pair correlation functions and cross-correlation functions (Waagepetersen et al., 2016) for the subprocesses, under certain assumptions. Some of these may fail to be easily computed or may not be interpretable (details in Section G of Supplementary Materials). To this end, we focus on the parameter estimates themselves, which provide a different way to quantify the clustering relationships among the multivariate processes.

As outlined in Section 3.1, parameters of primary interest in the proposed model are the α_l and h_l parameters, for $l = p + 1, \dots, p + q$. The α_l corresponds to how densely the l -th process clusters around its parent process. Higher values of α_l indicate denser clustering around the parent process. The bandwidth parameter, h_l determines how tightly the l -th process clusters around its parent process. A value of $h_l > h_0$ may indicate no or negligible clustering between the l -th process and its supposed parent process, where h_0 is a predetermined threshold based on the context of application. These parameters provide additional quantitative information about the relationship between a clustered process and its parent process, quantities not captured by the $K(r)$ function.

3.3. *Prior Distributions and Practical Considerations.* We outline priors for the unknown model parameters to complete the Bayesian specification of the MCP model. Specifically, we consider the following priors:

$$(5) \quad \begin{aligned} \alpha_l &\stackrel{iid}{\sim} \text{Gamma}(a_Y, b_Y), \quad l = p + 1, \dots, p + q, \\ h_l &\stackrel{iid}{\sim} \text{Half-Normal}(\sigma), \quad l = p + 1, \dots, p + q, \\ \lambda_v^C &\stackrel{iid}{\sim} \text{Gamma}(a_C, b_C), \quad v = 1, \dots, p, \\ \lambda_j &\stackrel{iid}{\sim} \text{Gamma}(a, b), \quad j = p + q + 1, \dots, m, \end{aligned}$$

where $\stackrel{iid}{\sim}$ denotes independent and identically distributed, and $(a, b, a_Y, b_Y, a_C, b_C, \sigma)$ are hyperparameters to be specified.

It is well appreciated in the literature on point process models that using a noninformative prior for spatial bandwidth or scale parameters is impossible due to numerical reasons, specifically, weak identifiability of the posterior distribution (Moller and Waagepetersen, 2003; Diggle, 2013; Kopecký and Mrkvička, 2016). We use a half-normal prior for the bandwidth parameters h_l ; ensuring the bulk of the mass remains on relatively small positive values enables comparatively easier prior elicitation. Specifically, the value of hyperparameter σ can be set such that the 99-th percentile of the half-normal prior corresponds to the maximum extent of the distance d between a parent point and offspring points. This choice helps sensitize the proposed Bayesian framework to stronger clustering within a small radius, which is the degree of clustering we seek to identify when, for example, cells of two bacterial taxa directly interact. In general, choosing the value of d should depend on the context of application.

3.4. *Computational Scheme.* Combining (3) and (5), the joint posterior density for the proposed MCP model can be written as

$$\pi(\boldsymbol{\theta}|Y) \propto L(Y|\boldsymbol{\theta})\pi(\boldsymbol{\theta}),$$

where $\pi(\boldsymbol{\theta})$ is the product of all the individual prior densities. We then proceed to draw samples from the posterior distribution by using a Markov chain Monte Carlo (MCMC) algorithm. Conventional NSP-type approaches treat the number of parent points and their locations as random and thus require an additional reversible jump MCMC step to estimate the parameters associated with the latent parent process (Green, 1995; Moller and Waagepetersen, 2003). In contrast, the proposed framework exploits the fact that the parent processes are observed and proceeds without a complex birth-death-move algorithm. The components of $\boldsymbol{\theta}$ can then be updated by Gibbs sampling (exploiting conjugacies in the full conditionals) or via Metropolis-Hastings steps (details in Section C of the Supplementary Material).

One practical challenge is that the integral term in (3) does not have a closed-form expression. Therefore, we use Monte Carlo methods to approximate the integral for computational

efficiency. In practice, the expression $\int_{\mathcal{W}} k_l(\mathbf{u} - \mathbf{c}_l, h_l) d\mathbf{u}$ can be thought of as the probability of occurrence of \mathbf{X}_l within the observation window \mathcal{W} , where \mathbf{X}_l is a bivariate real-valued random variable with density $k_l(\cdot - \mathbf{c}_l, h_l)$. Furthermore, in the proposed framework with Thomas processes, $k_l(\cdot - \mathbf{c}_l, h_l)$ corresponds to a bivariate normal density function with mean \mathbf{c}_l and covariance matrix $h_l^2 \mathbf{I}$. In this case, we draw samples from the bivariate normal distribution and compute the average proportion of points that fall within \mathcal{W} , which serves as an approximation to the integral term in (3).

We further optimized the code by using C language based coding. An R software package is available in the online repository at <https://github.com/SumanM47/MCPP.git>. The implementation of the model in the R package can generate 10,000 scans in 1.5 minutes for a dataset with ~ 150 points from a single parent process with a total of ~ 750 points from two offspring processes on a Dell Latitude 7210 laptop with i5 cores and 16 gigabytes of memory.

3.5. Model validation. We assess goodness-of-fit of the models by comparing the observed and estimated counts of different entities. Specifically, for the parent species, the estimated intensity parameter λ_v^C , $v = 1, \dots, p$, per unit area can be scaled by the area of the observation window. If the model is approximately correct, this quantity, $\lambda_v^C |W|$, should be close to the number of the v -th parent cells counted in the observation window. For approximating the l -th offspring count, one can compute the posterior mean of $\alpha_l \sum_{\mathbf{c} \in C_l} \int_{\mathcal{W}} k_l(\mathbf{u} - \mathbf{c}, h_l) d\mathbf{u}$ for $l = p + 1, \dots, p + q$. The integral term can be approximated by Monte Carlo method as described in Section 3.4. This expression involves both the offspring density parameter and the bandwidth parameter and therefore helps validate the joint estimate of the (α_l, h_l) pair. In our example, $\lambda^C |W|$ should provide a good estimate of the number of *Corynebacterium* cells; and $\alpha_2 \sum_{\mathbf{c} \in C_2} \int_{\mathcal{W}} k_2(\mathbf{u} - \mathbf{c}, h_2) d\mathbf{u}$, $\alpha_3 \sum_{\mathbf{c} \in C_3} \int_{\mathcal{W}} k_3(\mathbf{u} - \mathbf{c}, h_3) d\mathbf{u}$ and $\alpha_4 \sum_{\mathbf{c} \in C_4} \int_{\mathcal{W}} k_4(\mathbf{u} - \mathbf{c}, h_4) d\mathbf{u}$ should be close to the observed number of *Streptococcus* clustered around *Corynebacterium*, the observed number of *Porphyromonas* clustered around *Corynebacterium*, and the observed number of *Pasteurellaceae* clustered around *Streptococcus*, respectively.

4. Simulation Studies.

4.1. Simulation Set-up. We performed simulation studies to benchmark the performance of the MCPP model. For simplicity, the unit square was taken as the observation window. We generated data under the model outlined in Section 3, with $q = 2$ offspring taxa B and C around the same parent taxon A , which was the only parent taxon ($p = 1$). We considered twelve data scenarios (Table 1) that varied in terms of offspring density (α_2, α_3), bandwidth (h_2, h_3), and presence of a taxon spatially unrelated to the multilayered arrangement (hereinafter referred to as “unrelated” taxon). Throughout the scenarios, the intensity of the parent process (λ_1^C) and that of the process for the unrelated taxon (λ_4) were set to 150 and 95, respectively. For each of the twelve scenarios, we generated 100 images, each analyzed as an independent dataset.

4.2. Analysis Plan and Hyperparameters. We applied the following three approaches to each simulated dataset:

- (i) *MCPP-MO*: Multi-offspring taxa (A as the parent of B or C) were jointly analyzed in one framework using the MCPP.
- (ii) *MCPP-SO*: Two separate groups of taxa (A as the parent of B) and (A as the parent of C) were analyzed respectively using the MCPP.

- (iii) *NSP*: Ignoring the parent taxon A , only offspring taxa B and C were analyzed separately (by necessity, with the *NSP*). We applied the method of minimum contrast (Diggle, 2013), by using the R package `spatstat` (Baddeley, Rubak and Turner, 2015).

The parameters estimated by the three approaches have different interpretations. For example, the bandwidth parameter h_2 in *NSP* models from the analysis (iii) is interpreted as the distance scale for the unobserved cluster formed by the offspring taxon B , ignoring the observed parent taxon A . Despite this distinction, we included analysis (iii) using the *NSP* because it is among the most relevant cluster point process models applied to this class of problems. In simulation studies, we primarily focused on the numerical performance of the methods in estimating the parameters rather than on their interpretations.

For analyses (i) and (ii), we set the hyperparameters $(a_Y, b_Y, a_C, b_C, a, b)$ to 0.01. We set the hyperparameter σ to 0.02 so that the 99-th percentile of the prior distribution of h_l 's was approximately 0.05 (i.e. 5% of the length of the observation window). We used the posterior means as point estimates of the model parameters.

We estimated the offspring intensity (α_2, α_3) and bandwidth parameters (h_2, h_3) for the offspring processes (taxa B and C) and the intensity parameter (λ_1^C) for the parent process (taxon A). For both the MCP-based models, the presented statistics are the average of the posterior mean for the parameters for each of the datasets in a given scenario. We also computed the posterior standard deviation (SD) averaged over the 100 datasets for each scenario as well as the standard deviations of the posterior means of the estimates for the different datasets (SD_{EST}). With the *NSP*, no uncertainty measure is available for the individual estimates for each dataset, so we computed only the standard deviation of each estimate across the simulated datasets. However, the *NSP* method failed to converge for several datasets in multiple scenarios. We report the percentage of instances where estimates of parameters are not reliable due to the numerical issue for each scenario. Therefore, for the *NSP*, the average estimates and SE were computed based only on the datasets in which the model converged.

4.3. Primary Results. Results were very similar between the MCP-MO and MCP-SO models. Hereafter, we refer to tabular results from the MCP-MO analyses, and the descriptive results apply equally to both versions of the MCP. The MCP method performed well in estimating the true parameter values with both a small SD and a small SD_{EST} (Tables 2 and S.1 of Supplementary Materials). The *NSP* method often failed to converge, in up to 70% of datasets, depending on the scenario. When the *NSP* did converge, it produced results that were nonsensical, with SEs too high to give any credibility to these estimates.

For both methods, standard errors increased in the high-bandwidth scenarios compared with the low-bandwidth scenarios. The parent process intensities were also captured better by the MCP model than by the classical *NSP* model, especially in high-bandwidth scenarios. Lastly, performance of the MCP approach was not affected by the presence of a taxon spatially unrelated to the multilayered arrangement (Tables 2 and S.1 of Supplementary Materials).

4.4. Sensitivity Analyses. As explained in Section 3.3, we used a half-normal prior for the bandwidth parameter. We conducted comprehensive sensitivity analyses (detailed in Section E of the Supplementary Materials) to examine the extent to which conclusions are robust with respect to the choice of prior distribution for the bandwidth parameter. In these analyses, we compared parameter estimation performance under three different prior distributions: half-normal, uniform, and log-normal. In summary, the proposed framework was not sensitive to the choice of the prior distribution for the bandwidth parameter under scenarios with low-bandwidth. Under high-bandwidth data scenarios, however, elicitation of an informative prior seemed to help the proposed framework become more numerically stable, increasing power.

TABLE 1

A summary of twelve simulation scenarios considered in Section 4. The offspring density is controlled by setting $(\alpha_2, \alpha_3) = (1.5, 1)$ for ‘Sparse’, $(4, 3)$ for ‘Dense’ and $(4, 1)$ for ‘Mixed’ densities. Bandwidth ‘Low’ sets $(h_2, h_3) = (0.01, 0.02)$ and ‘High’ to $(0.1, 0.01)$. The setting “Unrelated taxon” refers to whether there exists a taxon in the data spatially unrelated to the multilayered arrangement.

Scenario	Unrelated taxon	Offspring density	Bandwidth
1	Absent	Sparse	Low
2	Absent	Sparse	High
3	Absent	Dense	Low
4	Absent	Dense	High
5	Absent	Mixed	Low
6	Absent	Mixed	High
7	Present	Sparse	Low
8	Present	Sparse	High
9	Present	Dense	Low
10	Present	Dense	High
11	Present	Mixed	Low
12	Present	Mixed	High

5. Analysis of Human Microbiome Biofilm Image Data. To illustrate the proposed methods, we analyzed microbiome biofilm image data described in Section 2. One challenge of biofilm image data is higher-order spatial structure, such as is evident in the image of a dental plaque biofilm community. Among other reasons for macro-level community structure, the environment at the outer edge of dental biofilm differs from that near the tooth surface. More locally, *Streptococcus* and *Porphyromonas* cluster around *Corynebacterium* only at its tip, not along its length and not at its base (Figure 3 and Mark Welch et al., 2016). Image sampling and processing further contribute to heterogeneity, especially in that the image is of a two-dimensional slice from a three-dimensional structure. Some areas of the image have a higher concentration of cross-sections in which *Corynebacterium* cells themselves appear spherical, whereas other areas display large numbers of lengthwise *Corynebacterium* filaments. Therefore, we qualitatively compared model performance when analyzing data from the whole image and data from the same image divided into four quadrants, each with more homogeneous spatial patterns than the whole.

5.1. Analysis of Whole Image Data.

5.1.1. *Hyperparameters and Analysis Settings.* From the $m = 9$ different taxa probed in the human dental plaque sample, we analyzed the data for locations of three offspring taxa, namely *Streptococcus*, *Porphyromonas* and *Pasteurellaceae*. The parent taxon for the first two taxa is *Corynebacterium* and for the third taxon, it is *Streptococcus* which itself is an offspring taxon (Figure 1). According to the notation introduced in Section 3.1, the process Y_1 corresponds to *Corynebacterium*, which functions only as a parent taxon ($p = 1$). Y_2 , Y_3 , and Y_4 represent the three offspring processes ($q = 3$) for *Streptococcus*, *Porphyromonas*, and *Pasteurellaceae*, respectively. The corresponding parent processes are $C_2 = Y_1$, $C_3 = Y_1$ (*Corynebacterium* as a parent), and $C_4 = Y_2$ (*Streptococcus* as a parent). The remainder of the taxa were modeled as homogeneous Poisson processes. In the MCPP analyses, we set the hyperparameters at $a_Y = b_Y = a_C = b_C = a = b = 0.01$ and σ at 0.97, such that the 99th percentile for the bandwidth parameters was approximately $2.5 \mu\text{m}$. The inclusion of black space, where no taxa are observed, can deflate density estimates and induce spurious spatial correlations. We minimized unnecessary black space by using a convex hull of the observed locations as the analysis window (Figure 5). We also applied the classical NSP model individually on the three offspring processes, *Streptococcus*, *Porphyromonas* and *Pasteurellaceae*.

TABLE 2

The true value, estimates (EST), and uncertainty measures for the offspring density (α_2 , α_3), bandwidth (h_2 , h_3), and parent process (λ^C) parameters from the MCCP-MO and NSP analyses in the first six simulated scenarios (those without any unrelated taxon). For the MCCP-MO model, the estimates are the posterior means averaged over different datasets, the SD is computed by averaging the posterior standard deviation over different datasets, and the SD_{EST} is computed as the standard deviation of the estimates over the datasets. For the NSP model, the estimates are the outputs of the minimum contrast method, and SE is calculated similarly by using these estimates. The SD for the NSP model is not computed, as the method does not provide an uncertainty measure. The last column (%F) refers to the percentage of datasets in which the NSP model failed to converge for a given scenario.

Scenario		True value	MCCP-MO			NSP		%F
			EST	SD	SD_{EST}	EST	SE	
1	α_2	1.50	1.54	0.10	0.11	2.34	7.71	6
	α_3	1.00	1.03	0.08	0.09	1.97	6.84	
	h_2	0.01	0.01	< 0.01	< 0.01	0.01	0.04	
	h_3	0.02	0.02	< 0.01	< 0.01	0.70	6.43	
	λ^C	150.00	164.07	13.16	13.28	170.78	52.51	
2	α_2	1.50	1.50	0.11	0.11	291.16	383.69	26
	α_3	1.00	1.02	0.08	0.08	1.06	0.40	
	h_2	0.10	0.08	0.01	0.01	8.33	23.82	
	h_3	0.01	0.01	< 0.01	< 0.01	0.01	< 0.01	
	λ^C	150.00	162.74	13.05	13.52	679.72	2378.68	
3	α_2	4.00	4.05	0.14	0.16	13.30	66.75	1
	α_3	3.00	3.06	0.13	0.11	10.60	75.03	
	h_2	0.01	0.01	< 0.01	< 0.01	0.02	0.10	
	h_3	0.02	0.02	< 0.01	< 0.01	0.03	0.08	
	λ^C	150.00	204.84	14.50	14.29	209.22	49.75	
4	α_2	4.00	4.01	0.17	0.17	710.62	648.03	56
	α_3	3.00	3.04	0.13	0.12	3.00	0.62	
	h_2	0.10	0.09	0.01	0.01	1.21	0.77	
	h_3	0.01	0.01	< 0.01	< 0.01	0.01	< 0.01	
	λ^C	150.00	202.08	14.34	15.32	20.33	45.79	
5	α_2	4.00	4.05	0.15	0.16	4.07	0.68	1
	α_3	1.00	1.03	0.17	0.09	3.06	14.91	
	h_2	0.01	0.01	< 0.01	< 0.01	0.01	< 0.01	
	h_3	0.02	0.02	< 0.01	< 0.01	1.10	10.15	
	λ^C	150.00	203.82	14.51	15.40	203.47	35.16	
6	α_2	4.00	4.02	0.17	0.14	685.54	694.99	53
	α_3	1.00	1.01	0.07	0.06	2.49	10.25	
	h_2	0.10	0.09	0.01	0.01	1.48	1.21	
	h_3	0.01	0.01	< 0.01	< 0.01	0.02	0.07	
	λ^C	150.00	198.19	14.22	13.86	35.99	99.33	

5.1.2. *Results.* For the MCCP, we ran three chains of length 3 million each with the initial 2 million iterations discarded as burn-in samples and the remaining samples thinned to obtain 10,000 posterior samples from each chain. The mixing was good for all the parameters. The estimates are posterior means and standard deviations based on the samples from all three chains. The NSP model was run separately for the three offspring taxa by using the R package `spatstat` based function `thomas.estK`, which uses the minimum contrast method to estimate the parameters. The procedure does not return any uncertainty estimates.

The MCCP approach successfully identified the multilayered arrangement in which *Streptococcus* and *Porphyromonas* clustered around *Corynebacterium* and *Pasteurellaceae* around *Streptococcus*. The MCCP-based bandwidth estimates for *Streptococcus* and *Porphyromonas* clustering around *Corynebacterium* are higher than expected but the same for *Pasteurellaceae*

TABLE 3

Results of MCPP and NSP analyses of human dental plaque biofilm data: estimates (EST) and uncertainty measures for the offspring density ($\alpha_2, \alpha_3, \alpha_4$), bandwidth (h_2, h_3, h_4), and parent process (λ^C) parameters. For the MCPP model, the estimates are the posterior means, and SD is computed as the posterior standard deviation for each of the parameters. For the NSP model, the estimates are the output of the minimum contrast method. SD is not computed for NSP, as the method does not provide one.

Parameter	MCPP		NSP
	EST	SD	EST
α_2	1.34	0.05	64.12
α_3	2.20	0.06	57.07
α_4	0.42	0.02	16.01
h_2	10.96	0.49	10.19
h_3	14.14	0.53	5.74
h_4	4.55	0.30	8.14
λ_1	0.02	< 0.01	< 0.01

clustering around *Streptococcus* is about what one would expect the bandwidth estimate to be (Table 3). The NSP estimates for the bandwidth parameters are lower but the offspring density parameters are huge. The estimated parameters from MCPP are consistent in the sense that the expected count computed using the parameters match the observed counts exactly when rounded to the nearest integer. The parameter estimates for the other taxa are presented in the Supplementary Material (Table S.3).

5.2. Analysis of Subsetted Image Data.

5.2.1. Analysis Plan. We subset the image in four equally sized quadrants (Figure 5) and analyzed data from each quadrant independently. While this ad hoc approach may be insufficient for some applications, testing and applying more optimal subsetting methods are beyond the scope of this work. The fact that taxa’s abundance varied across the quadrants allowed for some comparison of performance (Table 4). The hyperparameters were set similarly as before, and convex hulls were created for each of the quadrants. We also performed NSP-based analysis of the three offspring taxa separately for each quadrant.

TABLE 4

The abundance (counts) of bacterial taxa of interest in the human dental plaque sample image data and its four subdivided quadrants.

Taxon	Quadrant				Total
	I	II	III	IV	
<i>Actinomyces</i>	119	280	154	223	776
<i>Capnocytophaga</i>	512	755	574	573	2414
<i>Corynebacterium</i>	58	219	186	245	708
<i>Fusobacterium</i>	92	250	141	173	656
<i>Leptotrichia</i>	191	411	234	339	1175
<i>Neisseriaceae</i>	339	479	402	491	1711
<i>Pasteurellaceae</i>	53	130	76	106	365
<i>Porphyromonas</i>	227	525	269	420	1441
<i>Streptococcus</i>	98	379	163	249	889

5.2.2. Results. The estimated bandwidth parameters h_2, h_3 and h_4 for the four quadrants ranged between 7.62–11.23 μm , 7.23–15.21 μm and 3.82–4.62 μm , respectively. The corresponding estimated offspring density parameters α_2, α_3 and α_4 were between 1.04–2.22, 1.80–5.05 and 0.36–0.57, respectively. The estimated intensity parameter for the process related to *Corynebacterium* was 0.01–0.02 per unit area (Table 5). The estimates of intensity

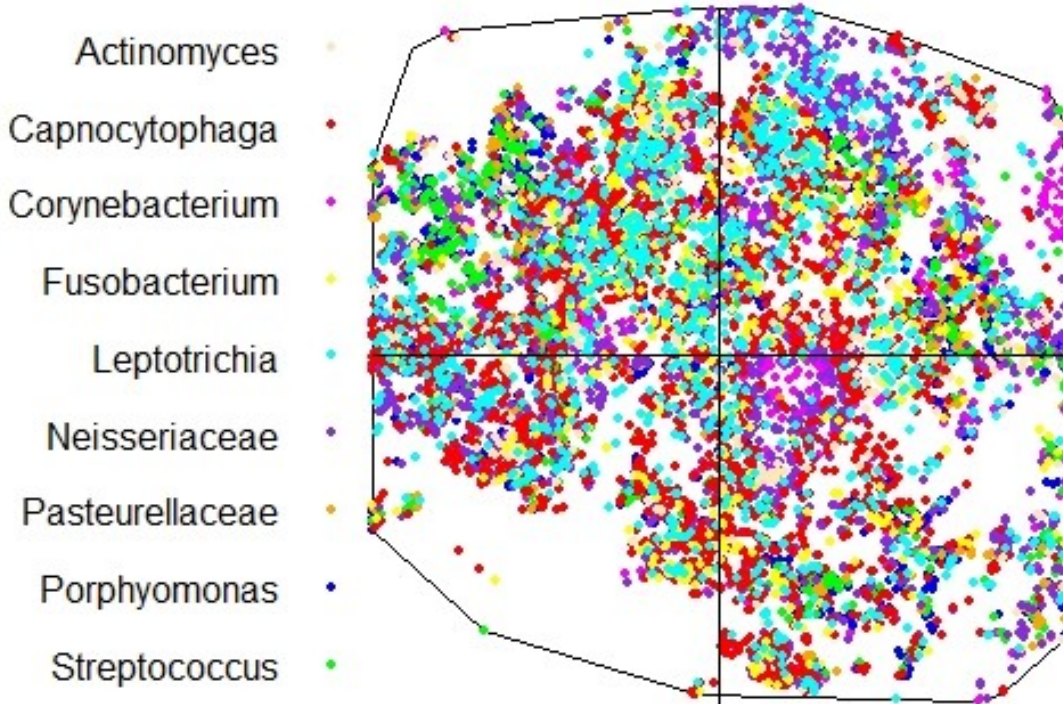


Fig 5: Division of the dental plaque sample image into the first (bottom left), second (top left), third (bottom right) and fourth (top right) quadrants. Black space has been removed.

parameters for the processes corresponding to the other taxa also varied among the quadrants (Supplementary Table S.3).

The estimates for the parent intensity and the offspring density parameters varied among quadrants and among the parent-offspring pairs. The estimates for λ^C in each quadrant were consistent with the observed counts. For example, in the second quadrant, there were 219 observed *Corynebacterium* cells, and the estimated intensity parameter of 0.02 per unit area corresponds to a count of ≈ 219 . For each of the three offspring taxa, the estimated counts matched the observed counts rounded to the nearest integer. For example, the estimated taxon counts for *Streptococcus*, *Porphyromonas* and *Pasteurellaceae* in the third quadrant compute to 163, 269 and 76 respectively, which match the corresponding observed counts (Table 4).

The estimated bandwidth parameters h_2 , h_3 and h_4 also varied by quadrant, exhibiting consistent patterns for the different offspring-parent pairs. The NSP analysis of each of the offspring processes resulted in very low estimated bandwidth parameter values (Table 5).

6. Discussion and Conclusion. We have developed a multivariate model to make inference about multiple parent-offspring clustering relationships simultaneously, including in the presence of multiple layers of clustering. The proposed MCP framework produces model parameters that directly quantify multiple structural arrangements, in which locations of one type of object depend on locations of another, central object. This task cannot be achieved with a traditional NSP approach because it ignores the locations of central “parent” objects. In simulation studies, the MCP based models produced less bias and much lower empirical standard deviations for parameter estimates compared with the NSP model, which produced rather nonsensical results. Although development of the proposed MCP model was motivated by oral microbiome biofilm image data, the approach is not specific to biofilm. The

TABLE 5

Results of MCPP and NSP analyses of human dental plaque biofilm data: estimates (EST) and uncertainty measures for the offspring density ($\alpha_2, \alpha_3, \alpha_4$), bandwidth (h_2, h_3, h_4), and parent process (λ^C) parameters from separate analyses of data from the four quadrants of the image. For the MCPP model, the estimates are the posterior means, and SD is computed as the posterior standard deviation for each of the parameters. For the NSP model, the estimates are the output of the minimum contrast method. SD is not computed for NSP, as the method does not provide one.

Segment	MCPP		NSP	
	EST	SD	EST	
I	α_2	2.22	0.22	9.94
	α_3	5.05	0.34	24.19
	α_4	0.57	0.08	15.39
	h_2	8.32	0.56	2.88
	h_3	7.23	0.50	2.55
	h_4	3.82	0.40	9.39
	λ^C	0.01	< 0.01	< 0.01
II	α_2	1.98	0.10	41.89
	α_3	2.91	0.13	35.43
	α_4	0.36	0.03	10.12
	h_2	11.23	0.58	7.07
	h_3	15.21	0.79	4.57
	h_4	4.23	0.46	6.72
	λ^C	0.02	< 0.01	< 0.01
III	α_2	1.04	0.08	9.34
	α_3	1.80	0.11	18.66
	α_4	0.52	0.06	3.78
	h_2	7.62	0.71	3.36
	h_3	9.83	0.72	1.92
	h_4	4.50	0.43	2.67
	λ^C	0.02	< 0.01	< 0.01
IV	α_2	1.22	0.08	32.29
	α_3	2.11	0.11	51.56
	α_4	0.46	0.05	9.93
	h_2	9.41	0.81	5.84
	h_3	11.09	0.72	4.14
	h_4	4.62	0.42	4.42
	λ^C	0.02	< 0.01	< 0.01

MCPP can be used in any image applications in which spatial dependencies reflect and provide information about the function of spatially arranged cells (or other objects) or about the function of arrangements themselves. Such applications could be biomedical, nonclinical, or nonbiological.

We demonstrated feasibility and utility of the proposed method in application to real biofilm image data that exhibit complex arrangements with nine taxa. Broadly speaking, the MCPP successfully captured the multilayered corn-cob-like structure among a group of four taxa, despite the presence of five other spatially unclustered taxa. Yet, the estimated bandwidth parameters were much greater than the approximately sub 5-micron distances expected from cell-to-cell (or nearly cell-to-cell) contact apparent in the visible corn-cob arrangements and likely when cells physico-chemically interact.

Because of this seeming discrepancy, it could be tempting to conclude that the low parent-offspring bandwidths estimated from the NSP framework make the NSP a more valid and preferred approach than the MCPP. However, because the classical NSP model ignores the location of parent cells, it highly underestimates the number of cluster centers (parents). To

compensate, it greatly overestimates the offspring density. Additionally, in ignoring parent locations, the NSP models self-clustering instead of parent-offspring clustering. Therefore, though seemingly appealing, the NSP produces estimates that are not appropriate to quantify the multilayered intertaxon relationships we sought to investigate.

It would also be inappropriate to interpret the MCP's high average estimated parent-offspring bandwidth strictly as bias or as reflecting a universal drawback to the proposed approach. Rather, the seeming discrepancy suggests the need for careful interpretation of model parameters from such a complex, heterogeneous image. It also highlights a need for modifications to the approach if a simple, direct interpretation about cell-to-cell (parent-to-offspring) contact is the goal.

Two characteristics of the dental plaque biofilm data present particular challenges. First, cells of *Corynebacterium* are filamentous. When the locations of imputed centroids are used to estimate average distances to neighboring cells of a different taxon, centroid-based methods may give misleading estimates of true cell-to-cell distances. This form of bias may be exacerbated by the specific biological organization, in that the spherical offspring taxa (*Streptococcus* and *Porphyromonas*) cluster around only one end of the parent *Corynebacterium* filaments. Estimates of average *Pasteurellaaceae-Streptococcus* distances were much smaller and closer to the expected range for cell-to-cell contact, likely because these clusters involved two types of similarly sized, spherical organisms.

One way to improve the MCP performance, therefore, might be to model the shapes of cells by bi-axial spheroids (Clem, Boysen and Rigaut, 1992) or elliptical cluster processes (Meinhardt et al., 2012). Another might be to use outline-based approaches, such as the Hausdorff distance (Huttenlocher, Klanderman and Rucklidge, 1993), rather than relying on the geographic coordinates of imputed centroids to locate each filamentous cell. Nevertheless, such complicated adaptations of the MCP approach are likely to be unnecessary if qualitative inference about the clustering arrangement suffices. Another option we are exploring is to condition models on features empirically identified in the image. Limiting the MCP analysis only to parent or offspring cells within some short distance of each other (e.g., radius = 10 microns) might improve its usefulness in similar applications, compared with analyses yielding only marginal bandwidth estimates over a heterogeneous spatial structure.

To explore another challenging feature, higher-order spatial structure, we analyzed subsetted image data. Between-quadrant variability in parameter estimates from both the MCP and NSP methods suggests the subsetting approach was helpful. Even more powerful would be incorporation of the MCP into a broader modeling framework that could capture higher-order spatial structure, for example, through regression parameters. The proposed model in (1) is flexible in that it can accommodate different standard modeling frameworks. For example, one can choose the form of $\lambda_i(\mathbf{s})$, $i = 1, \dots, m$, and replace the homogeneous Poisson process components in (2) by multivariate log-Gaussian Cox process components. Such an extension would enable the characterization and quantification of more complex spatial correlation structures among multiple taxa or other types of objects. We are currently developing these models.

We are also pursuing an avenue that will further enhance usefulness of the approach, by developing a meta-analytic framework to combine data from multiple images. In 100 sampled images of tongue biofilm from five donors, both within-sample and across-sample variability of inter-taxon spatial relationships is apparent (Wilbert, Welch and Borisy, 2020). This variability can be quantified via a meta-analytic, multivariate, log-Gaussian Cox process model that we have developed (manuscript in preparation). To date, it has not been standard to apply formal unified models to combine data across multiple biomedical images. Instead,

most practitioners have relied on post hoc comparisons, such as through ANOVA or non-parametric two-group comparisons. An efficient meta-analytic approach would also allow estimation and testing of covariate relationships with specific spatial structures, thereby increasing the scope and applicability of the proposed method.

Validation of MCPP models is not straightforward. Complex spatial structures generally do not permit out-of-sample prediction or split-sample cross-validation. In the context of traditional Bayesian point process models, the empirical spatial distributions can be compared with those based on posterior predictive samples (Leininger and Gelfand, 2017). However, this observed-versus-expected approach is challenged by the complexity of the data. Residuals for each of the sub-processes in (2) are easily obtained. Yet, a good match of observed and expected counts for one process can be misleading about overall model fit if another process is poorly estimated. This is exactly what happened with the NSP analysis of real data, where predicted offspring counts were accurate, and predicted parent counts were grossly underestimated. In contrast, the MCPP models produced nearly perfect prediction of counts of different taxa in the observation window. To our knowledge, there is as yet no valid method to combine the multiple residuals to produce a summary statistic reflecting overall goodness-of-fit.

We have proposed a novel MCPP method for quantifying multilayer, multivariate spatial relationships that we applied to analyze spatial arrangements of microbial cells in dental plaque biofilm image data. The proposed method exploits information about locations of objects at the center of a cluster of unlike objects, providing distinct advantages over the classic NSP model when information about locations of central “parent” objects is available. The MCPP model clearly outperformed the existing cluster point process model in every scenario in numerical studies.

Funding. The authors were funded by NIH grants GM126257, DE026872, DE027486, ES000002, DE016937 and DE022586. We are grateful for this support.

REFERENCES

- BADDELEY, A., RUBAK, E. and TURNER, R. (2015). *Spatial point patterns: methodology and applications with R*. CRC press.
- BORNANCINI, C. G., MARTÍNEZ, H. J., LAMBAS, D. G., DE VRIES, W., VAN BREUGEL, W., DE BREUCK, C. and MINNITI, D. (2004). Clustering and light profiles of galaxies in the environment of 20 ultra-steep-spectrum radio sources. *The Astronomical Journal* **127** 679.
- BORNANCINI, C. G., PADILLA, N. D., LAMBAS, D. G. and DE BREUCK, C. (2006). Spatial clustering of Ultra Steep Spectrum sources and galaxies. *Monthly Notices of the Royal Astronomical Society* **368** 619–622.
- BOURQUE, J. and DESROCHERS, A. (2006). Spatial aggregation of forest songbird territories and possible implications for area sensitivity. *Avian conservation and ecology* **1**.
- CHIU, S. N., STOYAN, D., KENDALL, W. S. and MECKE, J. (2013). *Stochastic geometry and its applications*. John Wiley & Sons.
- CLEM, C., BOYSEN, M. and RIGAUT, J. (1992). Towards 3-D modelling of epithelia by computer simulation. *Analytical Cellular Pathology: the Journal of the European Society for Analytical Cellular Pathology* **4** 287–301.
- CRESSIE, N. (2015). *Statistics for spatial data*. John Wiley & Sons.
- DAIMS, H., LÜCKER, S. and WAGNER, M. (2006). Daime, a novel image analysis program for microbial ecology and biofilm research. *Environmental microbiology* **8** 200–213.
- DIGGLE, P. J. (2013). *Statistical analysis of spatial and spatio-temporal point patterns*. CRC press.
- DIGGLE, P. J., MORAGA, P., ROWLINGSON, B. and TAYLOR, B. M. (2013). Spatial and spatio-temporal log-Gaussian Cox processes: extending the geostatistical paradigm. *Statistical Science* **28** 542–563.
- GREEN, P. J. (1995). Reversible jump Markov chain Monte Carlo computation and Bayesian model determination. *Biometrika* **82** 711–732.

- HARTMANN, R., JECKEL, H., JELLI, E., SINGH, P. K., VAIDYA, S., BAYER, M., RODE, D. K., VI-DAKOVIC, L., DÍAZ-PASCUAL, F., FONG, J. C. et al. (2021). Quantitative image analysis of microbial communities with BiofilmQ. *Nature microbiology* **6** 151–156.
- HILL, G. J. and LILLY, S. J. (1991). A change in the cluster environments of radio galaxies with cosmic epoch. *The Astrophysical Journal* **367** 1–18.
- HUTTENLOCHER, D. P., KLANDERMAN, G. A. and RUCKLIDGE, W. J. (1993). Comparing images using the Hausdorff distance. *IEEE Transactions on pattern analysis and machine intelligence* **15** 850–863.
- ILLIAN, J., PENTTINEN, A., STOYAN, H. and STOYAN, D. (2008). *Statistical analysis and modelling of spatial point patterns* **70**. John Wiley & Sons.
- JALILIAN, A., GUAN, Y., MATEU, J. and WAAGEPETERSEN, R. (2015). Multivariate product-shot-noise Cox point process models. *Biometrics* **71** 1022–1033.
- JONES, S. J. (1972). A special relationship between spherical and filamentous microorganisms in mature human dental plaque. *Archives of Oral Biology* **17** 613–IN27.
- KOPECKÝ, J. and MRKVIČKA, T. (2016). On the Bayesian estimation for the stationary Neyman-Scott point processes. *Applications of Mathematics* **61** 503–514.
- LEININGER, T. J. and GELFAND, A. E. (2017). Bayesian inference and model assessment for spatial point patterns using posterior predictive samples. *Bayesian Analysis* **12** 1–30.
- MARK WELCH, J. L., ROSSETTI, B. J., RIEKEN, C. W., DEWHIRST, F. E. and BORISY, G. G. (2016). Biogeography of a human oral microbiome at the micron scale. *Proceedings of the National Academy of Sciences* **113** E791–E800.
- MEINHARDT, M., LÜCK, S., MARTIN, P., FELKA, T., AICHER, W., ROLAUFFS, B. and SCHMIDT, V. (2012). Modeling chondrocyte patterns by elliptical cluster processes. *Journal of structural biology* **177** 447–458.
- MELLES, S., BADZINSKI, D., FORTIN, M.-J., CSILLAG, F. and LINDSAY, K. (2009). Disentangling habitat and social drivers of nesting patterns in songbirds. *Landscape ecology* **24** 519–531.
- MØLLER, J. (2003). Shot noise Cox processes. *Advances in Applied Probability* **35** 614–640.
- MØLLER, J., SYVERSVEEN, A. R. and WAAGEPETERSEN, R. P. (1998). Log gaussian cox processes. *Scandinavian journal of statistics* **25** 451–482.
- MOLLER, J. and WAAGEPETERSEN, R. P. (2003). *Statistical inference and simulation for spatial point processes*. CRC Press.
- MORILLO-LOPEZ, V., SJAARDA, A., ISLAM, I., BORISY, G. G. and WELCH, J. M. (2021). Corn cob structures in dental plaque reveal microhabitat taxon specificity.
- NEYMAN, J. and SCOTT, E. L. (1958). Statistical approach to problems of cosmology. *Journal of the Royal Statistical Society: Series B (Methodological)* **20** 1–29.
- RIPLEY, B. D. (2005). *Spatial statistics*. John Wiley & Sons.
- SCHINDELIN, J., ARGANDA-CARRERAS, I., FRISE, E., KAYNIG, V., LONGAIR, M., PIETZSCH, T., PREIBISCH, S., RUEDEN, C., SAALFELD, S., SCHMID, B. et al. (2012). Fiji: an open-source platform for biological-image analysis. *Nature methods* **9** 676–682.
- TANAKA, U. and OGATA, Y. (2014). Identification and estimation of superposed Neyman–Scott spatial cluster processes. *Annals of the Institute of Statistical Mathematics* **66** 687–702.
- TAROF, S. A. and RATCLIFFE, L. M. (2004). Habitat characteristics and nest predation do not explain clustered breeding in Least Flycatchers (*Empidonax minimus*). *The Auk* **121** 877–893.
- VORREGAARD, M. (2008). Comstat2-a modern 3D image analysis environment for biofilms, Master’s thesis, Citeseer.
- WAAGEPETERSEN, R., GUAN, Y., JALILIAN, A. and MATEU, J. (2016). Analysis of multispecies point patterns by using multivariate log-Gaussian Cox processes. *Journal of the Royal Statistical Society: Series C (Applied Statistics)* **65** 77–96.
- WILBERT, S. A., WELCH, J. L. M. and BORISY, G. G. (2020). Spatial ecology of the human tongue dorsum microbiome. *Cell reports* **30** 4003–4015.
- YATES, M., MILLER, L. and PEACOCK, J. (1989). The cluster environments of powerful, high-redshift radio galaxies. *Monthly Notices of the Royal Astronomical Society* **240** 129–166.

MULTIVARIATE CLUSTER POINT PROCESS MODEL: PARENT LOCATION IMPROVES INFERENCE FOR COMPLEX BIOFILM IMAGE DATA

BY SUMAN MAJUMDER^{1,a}, BRENT A. COULL^{1,b} JESSICA L. MARK WELCH^{2,d}
PATRICK J. LA RIVIERE^{3,e} FLOYD E. DEWHIRST^{4,f}
JACQUELINE R. STARR^{5,*g} AND KYU HA LEE^{1,*c}

¹Harvard T. H. Chan School of Public Health, Boston, Massachusetts, U.S.A., ^asmajumder@hsph.harvard.edu;
^bbcoull@hsph.harvard.edu; ^cklee@hsph.harvard.edu

²Marine Biological Laboratory, Woods Hole, Massachusetts, U.S.A., ^djmarkwelch@mbl.edu

³University of Chicago, Chicago, Illinois, U.S.A., ^epjlarivi@uchicago.edu

⁴The Forsyth Institute, Cambridge, Massachusetts, U.S.A., ^ffdewhirst@forsyth.org

⁵Brigham and Women's Hospital, Boston, Massachusetts, U.S.A., ^gspjst@channing.harvard.edu

CONTENTS

A	Neyman-Scott process	2
B	Images of the remaining taxa from the human dental plaque biofilm data	3
C	Computational details of the sampling algorithm	4
C.1	Updating parameters associated with offspring densities	4
C.2	Updating intensity parameters in homogeneous Poisson processes	4
C.3	Updating bandwidth parameters	4
D	Table of estimates for the remaining scenarios from the simulation study	5
E	Analysis of sensitivity of the MCPP-MO to choice of prior for the bandwidth parameters	6
F	MCPP-based parameter estimates for taxa not observed as part of corncob-like arrangements in dental plaque biofilm image data	7
G	Consideration for computing $K(r)$ function for MCPP	8

*Co-senior authors

A. Neyman-Scott process. A Neyman-Scott process is a point process used for modeling parent-offspring clustering. In the simplest setting, consider the parent process C to be a homogeneous Poisson point process with intensity λ^C . For each observation location $c \in C$, the cluster of offspring Y_c is an independent Poisson process with intensity $\alpha k(\cdot - c, h)$, where $k(\cdot - c, h)$ is a probability distribution function parametrized by h that determines the spread and distribution of the offspring locations around the parent c , and $\alpha > 0$ is the expected number of offspring per cluster. The Neyman-Scott process Y is the union of all these offspring cluster processes, namely, $Y = \bigcup_{c \in C} Y_c$. Further details can be found in ? and ?, for example.

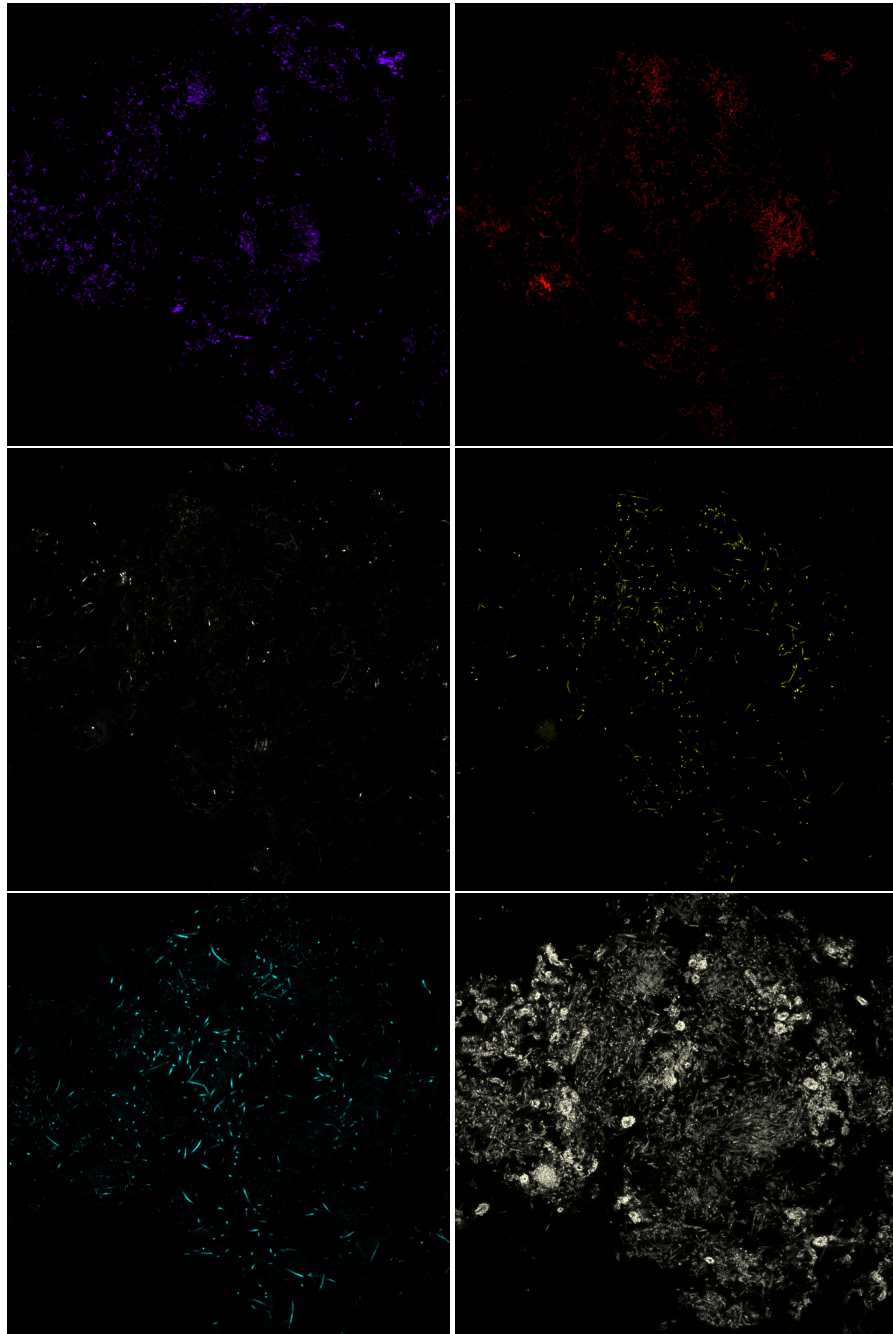
B. Images of the remaining taxa from the human dental plaque biofilm data.

Fig S.1: RGB images of *Neisseriaceae* (top left), *Capnocytophaga* (top right), *Actinomyces* (middle left), *Fusobacterium* (middle right), *Leptotrichia* (bottom left) and *Bacterium* (bottom right) in the dental plaque biofilm sample. *Bacterium* denotes a probe for all oral bacteria. It is used for methodologic purposes to evaluate the completeness of the set of specific probes. Hence, it is omitted from analysis of community spatial structure. The genera shown here were modeled as homogeneous Poisson process in the data analysis.

C. Computational details of the sampling algorithm. We use a Markov chain Monte Carlo (MCMC) method to draw samples from the joint posterior distribution of $\boldsymbol{\theta}$. In the MCMC scheme, parameters are updated by either exploiting conjugacies inherent to the proposed model or using a Metropolis-Hastings algorithm.

C.1. Updating parameters associated with offspring densities. Let $\boldsymbol{\theta}^{-(\alpha)}$ denote a set of parameters $\boldsymbol{\theta}$ with α removed. The full conditional distribution for α_l , $l = p + 1, \dots, p + q$ is

$$\alpha_l | \boldsymbol{\theta}^{-(\alpha_l)} \sim \text{Gamma}(a_Y + n_l, b_Y + \sum_{\mathbf{c}_l \in C_{lW}} \int k_l(\mathbf{u} - \mathbf{c}_l, h_l) d\mathbf{u}),$$

where n_l is the number of observations in the window of taxon l .

C.2. Updating intensity parameters in homogeneous Poisson processes. Posterior conjugacy is also achieved in the full conditional distributions of intensity parameters, λ_v^C , $v = 1, \dots, p$ and λ_j , $j = p + q + 1, \dots, m$, which are given by

$$\lambda_v^C | \boldsymbol{\theta}^{-(\lambda_v^C)} \sim \text{Gamma}(a_C + n_v, b_C + |\mathcal{W}|), \quad v = 1, \dots, p; \text{ and}$$

$$\lambda_j | \boldsymbol{\theta}^{-(\lambda_j)} \sim \text{Gamma}(a + n_j, b + |\mathcal{W}|), \quad j = p + q + 1, \dots, m;$$

where n_v and n_j are the numbers of observations for taxon v and taxon j within the window, respectively.

C.3. Updating bandwidth parameters. Since the full conditionals of the bandwidth parameters do not have standard forms, we use a random walk Metropolis-Hastings step to update each of h_l , $l = 1, \dots, p$. Denote $h_j^{(t)}$ the sample for h_j , $j = p + 1, \dots, p + q$ from iteration t . For iteration $(t + 1)$, we propose a candidate sample h_j^* as a random draw from $N(h_j^{(t)}, \sigma_{prop}^2)$, where σ_{prop}^2 is the prespecified variance of the proposal density. The corresponding acceptance ratio computes to

$$R = \frac{\exp\left(-\alpha_l \sum_{\mathbf{c}_l \in C_l} \int_W k(\mathbf{u} - \mathbf{c}_l, h_j^*) d\mathbf{u}\right) \prod_{\mathbf{y} \in Y_l} \left(\sum_{\mathbf{c}_l \in C_l} \int_W k(\mathbf{u} - \mathbf{c}_l, h_j^*)\right) \exp\left(-h_j^{*2}/2\sigma^2\right) \mathbb{I}(h_j^* > 0)}{\exp\left(-\alpha_l \sum_{\mathbf{c}_l \in C_l} \int_W k(\mathbf{u} - \mathbf{c}_l, h_j^{(t)}) d\mathbf{u}\right) \prod_{\mathbf{y} \in Y_l} \left(\sum_{\mathbf{c}_l \in C_l} \int_W k(\mathbf{u} - \mathbf{c}_l, h_j^{(t)})\right) \exp\left(-h_j^{(t)2}/2\sigma^2\right)}.$$

Then, we accept the proposed candidate h_j^* as $h_j^{(t+1)}$ with probability $\min\{R, 1\}$ or keep $h_j^{(t+1)} = h_j^{(t)}$.

TABLE S.1

The true value, estimates (EST), and uncertainty measures for the offspring density (α_2 , α_3), bandwidth (h_2 , h_3), and parent process (λ^C) parameters from the MCCP-MO and NSP analyses in the last six simulated scenarios (those with an unrelated taxon). For the MCCP model, the estimates are the posterior means averaged over different datasets, the SD is computed by averaging the posterior standard deviation over different datasets, and the SD_{EST} is computed as the standard deviation of the estimates over the datasets. For the NSP model, the estimates are the outputs of the minimum contrast method, and SE is calculated similarly by using these estimates. The SD for the NSP model is not computed, as the method does not provide an uncertainty measure. The last column (%F) refers to the percentage of datasets in which the NSP model failed to converge for a given scenario.

Scenario		True Value	MCCP-MO			NSP		%F
			EST	SD	SD_{EST}	EST	SE	
7	α_2	1.50	1.53	0.10	0.10	1.46	0.33	
	α_3	1.00	1.02	0.08	0.09	3.31	20.25	
	h_2	0.01	0.01	< 0.01	< 0.01	0.01	< 0.01	2
	h_3	0.02	0.02	< 0.01	< 0.01	0.04	0.09	
	λ^C	150.00	161.06	12.91	12.20	171.35	34.72	
8	α_2	1.50	1.48	0.11	0.09	198.46	283.69	
	α_3	1.00	1.02	0.08	0.09	0.98	0.28	
	h_2	0.10	0.08	0.01	0.01	10.30	28.72	36
	h_3	0.01	0.01	< 0.01	< 0.01	0.01	< 0.01	
	λ^C	150.00	160.25	12.86	12.57	939.70	2777.40	
9	α_2	4.00	4.02	0.14	0.15	8.77	48.78	
	α_3	3.00	3.05	0.13	0.13	2.91	0.77	
	h_2	0.01	0.01	< 0.01	< 0.01	0.02	0.08	0
	h_3	0.02	0.02	< 0.01	< 0.01	0.02	< 0.01	
	λ^C	150.00	202.78	14.38	14.29	208.52	39.37	
10	α_2	4.00	4.00	0.17	0.17	613.34	569.20	
	α_3	3.00	3.02	0.13	0.14	2.93	0.53	
	h_2	0.10	0.09	0.01	0.01	1.15	0.64	48
	h_3	0.01	0.01	< 0.01	< 0.01	0.01	< 0.01	
	λ^C	150.00	200.49	14.26	14.48	13.30	28.78	
11	α_2	4.00	4.05	0.15	0.14	18.45	87.48	
	α_3	1.00	1.00	0.07	0.08	2.05	10.04	
	h_2	0.01	0.01	< 0.01	< 0.01	0.03	0.11	0
	h_3	0.02	0.02	< 0.01	< 0.01	0.47	4.41	
	λ^C	150.00	201.50	14.37	14.09	203.36	53.30	
12	α_2	4.00	4.02	0.17	0.17	547.61	553.61	
	α_3	1.00	1.02	0.07	0.07	0.97	0.24	
	h_2	0.10	0.09	0.01	0.01	1.04	0.82	70
	h_3	0.01	0.01	< 0.01	< 0.01	0.01	< 0.01	
	λ^C	150.00	199.05	14.23	15.95	26.62	41.46	

D. Table of estimates for the remaining scenarios from the simulation study. Here we present the results from the remaining six scenarios considered in the simulation study that are not presented in the main document. The results obtained are similar to what was seen in Section 4 of the main document. The multivariate cluster point process (MCCP) performs better than the Neyman-Scott process (NSP) implementation in all aspects. NSP often fails to converge, especially in scenarios where the bandwidth parameter is large.

E. Analysis of sensitivity of the MCPP-MO to choice of prior for the bandwidth parameters . As part of the simulation study described in Section 4, we also evaluated the sensitivity of the MCPP-MO method to choice of prior distribution for the bandwidth parameters. Specifically, we considered four different prior distributions, namely 1) half-normal, 2) uniform, 3) log-normal with a flat tail and high variance and 4) log-normal with a slim tail and higher peak. For the uniform prior, the lower and upper bounds were taken to be 0 and 0.2, respectively. Both the log-normal priors had $\mu = \log 0.05$; the flat-tailed prior had $\sigma = 1$, and the high-peaked prior had $\sigma = 0.1$ as the hyperparameter. The hyperparameter setting for the half-normal prior was the same as in Section 4. In the sensitivity analyses, we compared performance of the MCPP with different prior distributions in Scenario 5 and 6 outlined in Table 1 of the main manuscript: both scenarios considered mixed offspring density ($\alpha_2=4$ and $\alpha_3=1$), one had low bandwidth ($h_2=0.01$ and $h_3=0.02$), and the other had high bandwidth ($h_2=0.1$ and $h_3=0.01$).

We report the mean absolute percentage bias for estimating the corresponding parameters in the two scenarios for the four different prior settings. The half-normal prior-based MCPP-MO model performed the best, and the performance was similar to what was observed in Section 4. When the true bandwidth was low, all the models, irrespective of prior choice, generally performed well and similarly to each other, with almost all biases $< 8\%$. Differences in performance emerged when the true bandwidth was high, where the analyses with tighter priors produced much less biased estimates ($< 10\%$ except in one instance) than the analyses with flatter priors (4-137%; Table S.2). However, using an informative log-normal prior backfired even for the low-bandwidth scenario when the offspring density was also low, as for the second offspring process ($\sim 20\text{-}25\%$).

TABLE S.2

Results of MCPP-MO based analysis of simulated data, comparing different choice of priors for the bandwidth parameters. The true values for the offspring densities were $\alpha_2=4$ and $\alpha_3=1$. The true values for the bandwidth parameters were $h_2=0.01$ and $h_3=0.02$ under low bandwidth and $h_2=0.1$ and $h_3=0.01$ under high bandwidth.

The parent process is denoted λ^C . Results are presented as mean absolute percentage bias of the estimated parameter values based on posterior means of each of the 100 simulated datasets. There were no other taxa unrelated to these multi-layered arrangements.

		Half-normal	Uniform	Log-normal (flat)	Log-normal (tight)
Low bandwidth	α_2	0.03	0.03	0.03	0.03
	α_3	0.07	0.07	0.07	0.07
	h_2	0.02	0.02	0.02	0.05
	h_3	0.04	0.04	0.04	0.24
	λ^C	0.06	0.06	0.06	0.06
High bandwidth	α_2	0.03	0.31	0.52	0.03
	α_3	0.05	0.05	0.05	0.05
	h_2	0.09	0.99	1.37	0.10
	h_3	0.03	0.03	0.03	0.20
	λ^C	0.06	0.06	0.06	0.06

F. MCCP-based parameter estimates for taxa not observed as part of corn-cob-like arrangements in dental plaque biofilm image data. Here we present the estimates for the modeling the distribution of the five taxa in the human dental plaque sample that are not associated with parent-offspring clustering, namely *Neisseriaceae*, *Capnocytophaga*, *Actinomyces*, *Fusobacterium* and *Leptotrichia*. Each was assumed to be distributed as a homogeneous Poisson process, and the corresponding intensity parameter in the entire image and in each of the quadrants is reported in Table S.3.

TABLE S.3

The posterior means of parameters associated with Neisseriaceae (λ_5), Capnocytophaga (λ_6), Actinomyces (λ_7), Fusobacterium (λ_8) and Leptotrichia (λ_9) obtained by applying the proposed MCCP method on the entire image and on each of the four quadrants of the dental plaque sample image. All results are rounded to two decimal places. The posterior standard deviations were all smaller than 0.01 and are not reported separately.

	λ_5	λ_6	λ_7	λ_8	λ_9
Full Image	0.04	0.06	0.02	0.02	0.03
Segment 1	0.04	0.06	0.01	0.01	0.02
Segment 2	0.05	0.07	0.03	0.02	0.04
Segment 3	0.04	0.05	0.01	0.01	0.02
Segment 4	0.05	0.06	0.02	0.02	0.03

G. Consideration for computing $K(r)$ function for MCPP. The superimposed process $Y(\mathbf{s})$ defined in Section 3.1 of the main manuscript has the intensity function

$$(1) \quad \lambda(\mathbf{s}) = \sum_{j=1}^M \lambda_j(\mathbf{s}) \mathbb{I}(\mathbf{s} \in Y_j),$$

where $\lambda_j(\mathbf{s})$ is the intensity of subprocess Y_j at location \mathbf{s} and $\mathbb{I}(\mathbf{s} \in Y_j)$ is the indicator function for the presence of a realization from Y_j at location \mathbf{s} . In order to obtain the theoretical $K(r)$ function for the process Y , one is required to compute the pair correlation function of Y between locations \mathbf{s} and \mathbf{s}' , which is defined as

$$(2) \quad g(\mathbf{s}, \mathbf{s}') = \frac{\mathbb{E}(\lambda(\mathbf{s})\lambda(\mathbf{s}'))}{\mathbb{E}(\lambda(\mathbf{s}))\mathbb{E}(\lambda(\mathbf{s}'))} = \frac{\mathbb{E}\left(\sum_{i=1}^M \sum_{j=1}^M \lambda_i(\mathbf{s})\lambda_j(\mathbf{s}')\mathbb{I}(\mathbf{s} \in Y_i)\mathbb{I}(\mathbf{s}' \in Y_j)\right)}{\mathbb{E}\left(\sum_{j=1}^M \lambda_j(\mathbf{s})\mathbb{I}(\mathbf{s} \in Y_j)\right)\mathbb{E}\left(\sum_{j=1}^M \lambda_j(\mathbf{s}')\mathbb{I}(\mathbf{s}' \in Y_j)\right)}.$$

Therefore, the form of $g(\mathbf{s}, \mathbf{s}')$ substantially depends on what is assumed for the membership of subprocesses at the locations through the indicator terms. For example, if we assume the same j_0 -th process at both locations \mathbf{s} and \mathbf{s}' , then $g(\mathbf{s}, \mathbf{s}')$ simply corresponds to the pair correlation function of subprocess Y_{j_0} between \mathbf{s} and \mathbf{s}' . On the other hand, if we assume that the subprocess Y_{j_0} is observed at location \mathbf{s} and another subprocess Y_{j_1} at location \mathbf{s}' , then $g(\mathbf{s}, \mathbf{s}')$ would be equivalent to the cross-correlation function between Y_{j_0} and Y_{j_1} at \mathbf{s} and \mathbf{s}' .

In conclusion, the pair correlation and cross-correlation functions may or may not have closed forms, as their forms rely on the choice of intensities for the subprocesses. Without additional assumptions on the membership of subprocesses at locations, derivation of the $g(\mathbf{s}, \mathbf{s}')$ and $K(r)$ function for superimposed process Y is intractable.